Marine Geology 397 (2018) 29–42

Contents lists available at ScienceDirect

Marine Geology

journal homepage: www.elsevier.com/locate/margo

A 9000-year flood history for Southern California: A revised stratigraphy of varved sediments in Santa Barbara Basin

Xiaojing Du[a], Ingrid Hendy[a,*], Arndt Schimmelmann[b]

[a] Department of Earth and Environmental Science, The University of Michigan, 2534 C.C. Little Building, 1100 North University Avenue, Ann Arbor, MI 48109, USA
[b] Department of Earth and Atmospheric Sciences, Indiana University, 1001 E 10th Street, Bloomington, IN 47405-1405, USA

ARTICLE INFO

Editor: G.J. de Lange

Keywords:
Radiocarbon chronology
Sedimentation rate
Flood event
Turbidity
Earthquake

ABSTRACT

The center of Santa Barbara Basin (SBB) preserves annual laminations through most of the Holocene providing an important locality for high-resolution late Quaternary paleoclimate and paleoceanography reconstructions. An accurate chronology is necessary for these sediment-based records and enables comparisons with more distal data time-series of similar quality. Here we present an improved high-resolution radiocarbon chronology for the last 9000 yrs. based on 89 accelerator mass spectrometric (AMS) ^{14}C dates of mixed planktonic foraminiferal carbonate from three sediment cores collected in SBB (MV0811-14JC, SPR0901-06KC and ODP Hole 893A). Accurate core-to-core correlation is demonstrated using prominent gray flood and olive turbidite layers identified in SBB and dated in multiple cores. Gray layer deposits were found more frequently in wetter intervals as determined by multi-proxy hydroclimate records in Southern California (e.g., lake deposits and tree rings). Mass accumulation rates (MARs) calculated for the SBB depocenter using the improved radiocarbon age model indicate high MARs are associated with these gray layers that have been associated with floods. Thus sediment accumulation in SBB is largely controlled by sediment delivery via river runoff following precipitation events although MARs may also be influenced by other factors that enhance erosion in river catchments. Folded sediment is observed within the basal core section of MV0811-14JC which stratigraphically correlates with ^{14}C age reversals in ODP Hole 893A. We associate this sediment slump feature with the large Goleta submarine slide complex in Santa Barbara Channel and estimate the submarine slide event occurred at ~ 9000 ± 200 yrs. BP. Furthermore, small olive turbidite layers identified and dated in SBB can be temporally linked with large earthquakes along San Andreas Fault and can therefore potentially reconstruct earthquake history in Southern California.

1. Introduction

The study of Holocene paleoclimate is crucial for understanding climate variability from millennial to interannual time scales (Mayewski et al., 2004; Wanner et al., 2008). The sediment record at the depocenter of Santa Barbara Basin (SBB) offshore of Southern California has been the basis of several paleoclimate and paleoceanography reconstructions (e.g. Lange et al., 1987; Kennett and Venz, 1995; Heusser, 1998; Schimmelmann et al., 2006). The predominantly annually laminated sediment record in SBB during the Holocene has the potential to resolve decadal and even interannual-to-annual paleoenvironmental and paleoceanographic changes (Weinheimer and Cayan, 1997; Hendy et al., 2015). However, an accurate chronology is needed to provide a time scale for SBB sediments and is essential for detailed comparisons with other paleoclimatic and paleoceanographic records.

Numerous investigations of SBB sediments chronology have taken place over the past 40 yrs. Soutar and Crill (1977) developed a chronology for 19th and 20th century SBB sediment based on annual layer/lamination or varve counting and ^{210}Pb dating. The establishment of a precise varve chronology and core-to-core correlation for the 19th century was followed by a detailed description of the ODP Hole 893A (34°17.25′N 120°02.2′W) varve stratigraphy (Lange and Schimmelmann, 1995). Additionally a number of AMS ^{14}C dates have been produced using mixed planktonic foraminiferal carbonate from ODP Hole 893A samples with 31 dates from the Holocene (Ingram and Kennett, 1995; Roark et al., 2003). Schimmelmann et al. (2006) expanded the chronology of partially varved sediment to the past 6700 yrs. using piston core 6P based on varve counting and ^{14}C–AMS dating. However, disagreements were found when comparing the traditional varve-count-based chronology to independent ^{14}C dates of planktonic foraminifera in multiple cores (Schimmelmann et al., 2006;

* Corresponding author.
E-mail addresses: xjdu@umich.edu (X. Du), ihendy@umich.edu (I. Hendy), aschimme@indiana.edu (A. Schimmelmann).

https://doi.org/10.1016/j.margeo.2017.11.014
Received 15 May 2017; Received in revised form 8 November 2017; Accepted 23 November 2017
Available online 28 November 2017
0025-3227/

Fisler and Hendy, 2008).

The discrepancy between SBB varve and ^{14}C chronologies may be explained by variations in the radiocarbon reservoir age of the regional surface ocean water and/or undercounting of annual layers in the varve chronology. Loss of varves (under-counting of absolute years) could be caused by erosion of varves and/or laminations being not consistently produced during drought intervals (Schimmelmann et al., 2006; Hendy et al., 2013; Schimmelmann et al., 2013). To resolve these issues a new high-resolution ~2000-yr chronology was developed using a combination of organic carbon ^{14}C dates from terrestrial floral macrofossils such as seeds, leaves, charcoal, and twigs and closely sampled planktonic foraminiferal carbonate ^{14}C dates (Hendy et al., 2013). Age differences between the ^{14}C planktonic foraminiferal carbonate and terrestrial organic carbon chronologies revealed variable reservoir ages (ΔR) while increasing offset between the ^{14}C and varve chronologies indicated a cumulative varve count error through the last 2000 yrs. Hendy et al. (2013) produced an improved chronology for SBB sediments with a variable ΔR applied to 49 mixed planktonic foraminiferal carbonate ^{14}C dates, however the chronology does not extend through the remainder of the Holocene.

Here we extend the high-resolution 2000-yr ^{14}C SBB chronology (Hendy et al., 2013) to 9000 yrs. BP (Before Present or before 1950 CE). Fifty new mixed planktonic foraminiferal carbonate ^{14}C dates were produced from jumbo piston core MV0811-14JC. In addition, we created a stratigraphy of 'instantaneous' gray flood and olive turbidite layers in SBB based on highly resolved imaging of core MV0811-14JC. We then employed this stratigraphy to correlate MV0811-14JC with ODP Site 893 and SPR0901-06KC such that the planktonic foraminiferal carbonate ^{14}C dates from these cores could be incorporated into a new master chronology for SBB sediments. Our new chronology is applied to the dated stratigraphic pattern of gray and olive layers and therefore can be applied to any future newly acquired SBB sediment cores to provide an easily accessible chronology for forthcoming paleoclimate studies. Finally we relate the gray flood and olive turbidite layers to regional paleoclimate reconstructions and tectonic activity.

2. Regional setting of SBB

Located off the southern coast of California, SBB is a tectonic depression representing the submerged southwestern part of the Transverse Ranges Province (Fig. 1). Late Quaternary sediments deposited in SBB are mostly composed of laminae couplets including biogenic (e.g., diatoms, radiolaria, planktonic and benthic foraminifera) and terrigenous sediments (Fleischer, 1972; Kolpack and Drake, 1984; Kennett and Venz, 1995; Rack and Merrill, 1995). Terrigenous sediments are delivered to SBB by rivers and streams (the Santa Clara and Ventura rivers and the Santa Ynez Mountains). The rivers and streams drain the tectonically active Western Transverse Ranges that are uplifting at rate of < 5 mm/yr (Duvall et al., 2004) producing an unusually high sedimentation rate (Thunell, 1998; Romans et al., 2009; Warrick and Mertes, 2009).

Southern California has a semiarid Mediterranean climate with cool winters and hot dry summers. Terrigenous material is delivered to SBB during winter precipitation events resulting in detrital siliciclastic sedimentation (dark laminae in X-radiographs) (Warrick et al., 2007) while biogenic sedimentation (light laminae in X-radiographs) occurs during the highly productive spring and summer seasons (Hülsemann and Emery, 1961). The northward migration of the North Pacific High Pressure System during the spring season positions strong northerly winds over the California coast and causes intense coastal upwelling (Lynn and Simpson, 1987). This imports nutrients into the photic zone and drives high regional biological productivity and the deposition of biogenic laminae. Suboxic bottom water in the deep center of the SBB renders the seafloor inhospitable to benthic macrofauna and prevents bioturbation allowing the seasonal variations in sedimentation to be preserved as annual laminae couplets (Behl, 1995; Schimmelmann et al., 2016). Thus the production and preservation of annual laminations provide the scientific basis for a varve chronology in SBB.

3. Methods

3.1. Radiocarbon dating

Samples 2 cm in thickness were collected at ~20 cm intervals over a total length of 980 cm from jumbo piston core MV0811-14JC (34° 16.906′N 120° 02.162′W; 580 m water depth; Fig. 1). Sediment samples were oven-dried, washed and wet sieved to retain the > 63 μm size fraction. Mixed planktonic foraminifera primarily consisting of *Globigerina bulloides* and *Neogloboquadrina incompta* were picked from the > 150 μm size fraction in each sediment sample to generate 50 carbonate ^{14}C dates (Table 1). Following standard methods, approximately 11 mg of foraminiferal shells were first leached in dilute HCl, then rinsed using Milli-Q water, dried and hydrolyzed using 85% phosphoric acid to produce CO_2 (Beverly et al., 2010). The resulting CO_2 was extracted, purified and graphitized using vacuum lines with H_2 gas and iron catalyst powder. Both pre-treatment and high-precision accelerator mass spectrometry (AMS) dating were performed at the Keck Carbon Cycle Accelerator Mass Spectrometer at the University of California Irvine.

3.2. Age-depth model

Gray and massive olive layers were logged in cores MV0811-14JC, SPR0901-06KC (34°16.914 N 120°02.419 W; 591 m water depth) and ODP Hole 893A (34°17.25′N 120°02.2′W; 588 m water depth) to create a master stratigraphy. Since flood layers and turbidites represent 'instantaneous' sedimentary events (Hendy et al., 2013; Schimmelmann et al., 2013) the thicknesses of the gray and olive layers were subtracted from the original core to create a corrected depth scale that incorporates only regular background sedimentation (typically laminated) (Table 1). The gray and olive layers were then used as stratigraphic tie points to correlate SPR0901-06KC and ODP Hole 893A depths to the MV0811-14JC depth scale (Table 2). A new composite corrected depth scale was generated so that the 49 ^{14}C dates from SPR0901-06KC (Hendy et al., 2013) and the 10 ^{14}C dates from core ODP Hole 893A (Roark et al., 2003) could be combined with the 50 MV0811-14JC ^{14}C dates.

An age-depth model from 46 to 9066 yrs. BP was generated using the software BACON2.2 (Blaauw and Christen, 2011). BACON uses Bayesian statistics to reconstruct coherent accumulation histories for deposits by combining radiocarbon dates with known sedimentary information (Blaauw and Christen, 2011) (Fig. 2). In this age model ^{14}C dates from cores SPR0901-06KC (Hendy et al., 2013) MV0811-14JC and ODP Hole 893A (Roark et al., 2003) were converted to calendar ages using the Marine13 calibration curves (Reimer et al., 2013). A variable reservoir age was applied to ages younger than 2000 yrs. BP where constraints were available (Hendy et al., 2013). Beyond 2000 yrs. BP a constant ΔR of 147 ± 70 yrs. was applied based on an estimate from the last constrained surface ocean reservoir age (Hendy et al., 2013). Eleven out of 49 ^{14}C ages from SPR0901-06KC, 6 out of 50 MV0811-14JC ^{14}C dates, and 3 out of 10 from core ODP Hole 893A (indicated as open symbols in Fig. 3) fell outside the age-depth line and were not used in this age model.

The ^{14}C plateaus during the last 300 yrs. preclude good calendar year calibration of ^{14}C dates in the youngest sediment sequence. Instead, previously published varve chronology data were employed after correlating stratigraphic marker layers between cores. These marker layers were previously identified in other box and kasten core studies (Schimmelmann et al., 1992; Hendy et al., 2013) and include: the coretop (1905 CE), a gray layer at 1861–62 CE, the *Macoma* layer at 1841 CE, a turbidite at 1811 CE and a gray layer at 1761 CE. Radiocarbon dates were employed downcore of the 1761 CE gray layer

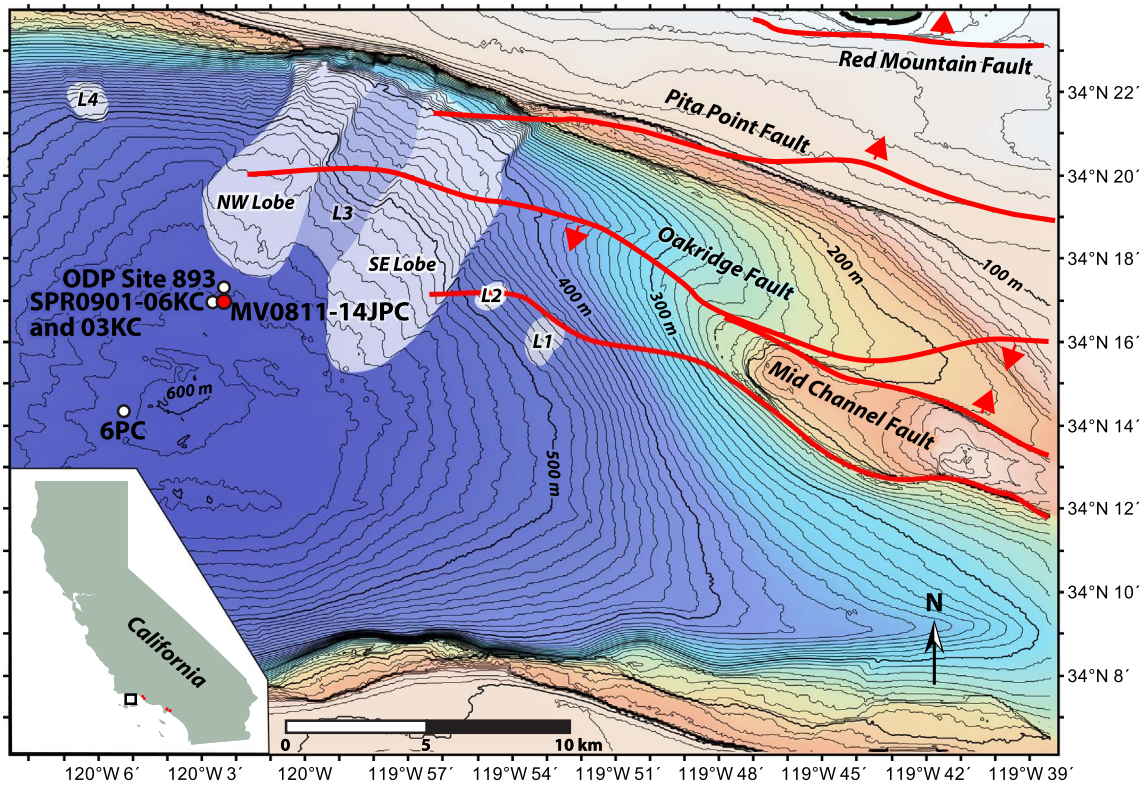

Fig. 1. Map of Santa Barbara Basin displaying the location of cores MV0811-14JC (filled red circle) ODP site 893 SPR0901-06KC 03KC and 6PC. Gray shading indicates the location of underwater slides denoted by the lettered numbers L1–4: L3 is the Goleta landslide complex and L4 is the Gaviota mudslide. The Goleta landslide complex includes two main surficial lobes: the northwest (NW) lobe and the southeast (SE) lobe (Fisher et al., 2005). Red lines show fault lines with arrows indicating direction of movement (adapted from Heck, 1998; Marshall et al., 2017). Bathymetric lines are 10 m apart with 100 m intervals marked by thick lines. Paleoseismological record locations are shown as red dots on the inset figure (from north to south: Pitas Point, Ventura, Los Angeles Basin and Seal Beach salt marsh). (For interpretation of the references to colour in this figure legend, the reader is referred to the web version of this article.)

(Table 3). Radiocarbon dates were not incorporated in the age model if they were associated with gray or olive layers or if they demonstrated stratigraphic inversion. Thus 89 ^{14}C total dates from the three sediment cores and five calendar ages were used in the Bayesian statistics of BACON 2.2 (Blaauw and Christen, 2011) to generate a new age model spanning the Holocene in SBB (Fig. 2). Sedimentation rates (SR in mm/yr) were calculated every 5 cm from the BACON 2.2 generated age model. Bulk mass accumulation rates (MAR in g cm^{-2} ka^{-1}) were calculated as the product of SR and dry bulk density (DBD in g cm^{-3}). Dry bulk density was generated using:

$$DBD = (1 - P/00) \times \rho$$

where P is porosity and ρ is density.

3.3. Bulk elemental analysis

Core MV0811-14JC was sampled at a variable spacing of 2–10 cm to generate 10 cm^3 bulk samples for elemental analyses. Samples were freeze dried, powdered and digested with hydrofluoric, nitric, perchloric and hydrochloric acids. Inductively coupled plasma-mass spectrometry (ICP-MS) and inductively coupled plasma-atomic emission spectroscopy (ICP-AES) were used to determine the elemental concentrations of major minor and trace element at ALS Laboratories in Vancouver Canada. The standard errors (1 st. err.) of measurements of lab standards GBM908-10 and MRGeo08 are ± 0.06 and ± 0.03% for calcium (Ca) and are ± 0.01% and ± 0.01% for titanium (Ti).

4. Results

4.1. Radiocarbon chronology

In Fig. 4 the mixed planktonic foraminiferal ^{14}C dates of core MV0811-14JC (Table 1) are plotted against a depth scale that has not been corrected for instantaneous sedimentation events in SBB. Dates generally exhibit increasing age with depth except those associated with instantaneous sedimentary structures. The trend of increasing age with depth weakens when dates straddle gray or olive layers. For example the section of MV0811-14JC between ~410 and 450 cmbct (cm below core top) contains three gray layers and two olive layers and the ^{14}C dates indicate that 40 cm of sediment was deposited in ~60 yrs. (sedimentation rate is ~ 1.5 yr cm^{-1}). However, for segments without instantaneous sedimentary events such as between ~490 and 510 cmbct the sedimentation rate is ~8.7 yr cm^{-1}.

Radiocarbon dating in MV0811-14JC was not undertaken beyond 870 cmbct (~60 cm depth in MV0811-14JC-sec 8) due to evidence of core disturbance (e.g., observed folds in laminations). This segment of MV0811-14JC corresponds to ~145 to 150 cmbct in ODP Hole 893A section 2H-05 and 0 to ~90 cmbct in section 2H-06 where ^{14}C age reversals are observed (Table 1). These radiocarbon age reversals in ODP Hole 893A occur between 8600 and 9610 ^{14}C yrs. and are calibrated to 9070–10,325 yrs. BP.

4.2. Gray and olive layer stratigraphy

Gray and olive layers were identified in multiple cores (core MV0811-14JC and ODP Site 893) through visual examination based on colour and sedimentary structure as well as elemental composition when available (i.e. MV0811-14JC). Gray layers range in thickness

Table 1
Raw radiocarbon dates (yrs BP) for planktonic foraminifera samples (with age uncertainties), uncorrected depth in core, depth corrected for instantaneous event thickness, calibrated ages (Cal yrs. BP) and 1 sigma range of calibrated ages (Cal yrs. BP). The calibrated age and 1 sigma range are calculated using CALIB 7.1 radiocarbon calibration program.

Sample name (Core section interval/cm)	Uncorrected depth (cm below core top)	Corrected depth (cm below core top)	Raw ^{14}C age (yrs)	Error (± yrs)	Calibrated age (Cal yrs. BP)	2σ age range
MV0811-14JC-						
Sec1 33–34[a]	33.0	23.2	2500	30	1979	1782–2181
Sec1 49–50.5	49.0	35.9	2645	15	2161	1977–2324
Sec1 58–60	58.0	40.8	2680	15	2200	1999–2345
Sec1 68–70	68.0	48.9	2745	15	2271	2081–2477
Sec1 80–81	80.0	57.9	2915	30	2507	2324–2699
Sec2 15–16	100.0	70.6	2990	35	2585	2359–2745
Sec2 114–116	114.0	84.4	3135	15	2768	2596–2953
Sec2 58–59	143.0	98.6	3325	30	2977	2776–3175
Sec2 154–156	154.0	102.2	3415	15	3093	2896–3306
Sec2 174–176	174.0	116.2	3460	15	3154	2953–3342
Sec2 182.5–185.5	182.5	122.0	3590	15	3313	3124–3494
Sec2 204–205	204.0	136.6	3780	15	3535	3358–3715
Sec2 124[a]	209.0	141.6	3515	30	3225	3004–3405
Sec2 214–216	214.0	146.6	3915	15	3706	3512–3895
Sec3 13–14[a]	241.0	166.9	4115	30	3969	3753–4200
Sec3 242–244	242.0	167.9	4085	15	3928	3718–4131
Sec3 282–284	282.0	188.9	4225	20	4119	3906–4345
Sec3 65–66	293.0	199.8	4315	30	4245	4002–4439
Sec3 304–306	304.0	208.3	4365	15	4310	4102–4505
Sec3 332–334	332.0	222.3	4475	15	4463	4241–4689
Sec3 362–364	362.0	244.8	4670	15	4712	4506–4871
Sec3 135	363.0	245.8	4670	35	4710	4493–4903
Sec3 382–384	382.0	264.8	4810	15	4901	4692–5134
Sec4 12–14	391.0	276.8	4995	15	5141	4905–5314
Sec4 32–34	411.0	294.4	5170	20	5379	5219–5567
Sec4 72–74	451.0	312.5	5230	15	5440	5291–5579
Sec4 91–93	470.0	328.4	5400	15	5618	5452–5794
Sec4 112–114	491.0	349.2	5585	20	5806	5637–5967
Sec4 132–134	511.0	369.2	5760	20	6017	5863–6195
Sec5 12–14	509.5	382.3	5965	15	6235	6052–6394
Sec6 14–16	539.3	397.6	6195	15	6470	6303–6633
Sec6 36–38	561.3	415.7	6415	15	6723	6540–6905
Sec6 45–47	570.3	424.3	6450	15	6764	6591–6948
Sec6 55–57	580.3	430.6	6515	20	6839	6651–7028
Sec6 74–76	599.3	438.6	6570	20	6908	6728–7122
Sec6 93–95	618.3	455.9	6710	20	7076	6898–7243
Sec6 104–106	629.3	466.9	6815	20	7196	7004–7356
Sec6 135–137[a]	660.3	479.2	7055	20	7418	7279–7551
Sec7 4–6[a]	676.5	492.9	6955	20	7331	7182–7456
Sec7 4–6[a]	676.5	492.9	6750	15	7121	6938–7274
Sec7 24–26	696.5	512.9	7155	20	7502	7382–7635
Sec7 44–46	716.5	525.5	7420	15	7738	7597–7896
Sec7 64–66	736.5	541.7	7590	15	7901	7731–8052
Sec7 86–88	758.5	562.3	7750	15	8064	7918–8224
Sec7 106–108	778.5	582.3	7995	20	8310	8154–8454
Sec7 126–128	798.5	600.7	8105	20	8422	8281–8582
Sec7 146–148	818.5	616.5	8260	20	8586	8399–8809
Sec8 8–10	830.5	625.7	8260	15	8586	8400–8805
Sec8 26–28	848.5	641.2	8445	15	8843	8605–9018
Sec8 47–49	869.5	656.7	8555	20	9009	8764–9235
146-893A-						
2H-05 146–148	NA	NA	8860	50	9373	9147–9527
2H-06 48–51	NA	NA	8950	100	9465	9138–9789
2H-06 55–57	NA	NA	8680	80	9168	8917–9441
2H-06 55-57B	NA	NA	9040	160	9599	9186–10,117
2H-06 73–75	NA	NA	8880	60	9392	9134–9550
2H-06 76–79	NA	NA	9610	70	10,325	10,121–10,569
2H-06 93–95	NA	NA	8600	60	9071	8770–9325

[a] Dates not included in the age model.

from 1 mm to > 15 cm and are typically fine-grained, sharp-based and contain high Ti concentrations (average Ti wt% ~ 0.45 ± 0.02) and low Ca/Ti elemental ratios (average Ca/Ti ~ 4.10 ± 0.68) compared to laminated sections (average Ti wt% ~ 0.37 ± 0.02 average Ca/Ti ~ 12.50 ± 1.34) (Table S1 in Supplemental materials). Most gray layers are homogenous but some (notably the thicker gray layers) are not and are instead composed of multiple closely-spaced thin layers that are distinguished by changes in colour and sedimentary structure (Fig. 5).

Olive layers are not laminated and range in thickness from 1 mm to ~10 cm and have sharp bases. Compared to gray layers, olive layers contain lower Ti concentrations (average Ti wt% ~ 0.38 ± 0.01) and higher Ca/Ti elemental ratios (average Ca/Ti ~ 10.66 ± 0.91) (Table S1 in Supplemental materials). Benthic foraminiferal sands are observed at the base of some olive layers such as 1B and 3A (Fig. S1 in Supplemental materials).

Table 2
BACON 2.2 input used in the age model construction.

Lab ID	Age	Error	Depth	Mean reservoir age (yrs)	1 standard deviation error
Varve_1.01	45	0	0.1	0	0
Varve_4.01	89	0	3.8	0	0
Varve_7.99	109	0	5.8	0	0
Varve_7.100	139	0	12.6	0	0
Varve_21.44	189	0	19.8	0	0
SPR09-06KC 10	790	45	8.8	304	70
SPR09-06KC 15	860	30	13.8	319	70
SPR09-06KC 20	890	30	18.8	343	70
SPR09-06KC 25	885	30	21.8	346	70
SPR09-06KC 31	885	30	22.8	347	70
SPR09-06KC 35	955	30	26.8	347	70
SPR09-06KC 45	985	30	36.8	347	70
SPR09-06KC 50	1075	30	41.8	347	70
SPR09-06KC 55	1110	30	46.8	336	70
SPR09-06KC 59	1100	30	46.8	336	70
SPR09-06KC 65	1175	30	51.8	323	70
SPR09-06KC 75	1250	30	61.8	297	70
SPR09-06KC 80	1345	30	66.3	285	70
SPR09-06KC 85	1425	30	71.3	272	70
SPR09-06KC 95	1425	30	76.3	259	70
SPR09-06KC 100	1505	30	81.3	246	70
SPR09-06KC 105	1570	30	86.3	233	70
SPR09-06KC 115	1555	30	91.3	219	70
SPR09-06KC 120	1620	30	96.3	206	70
SPR09-06KC 126	1705	30	102.3	191	70
SPR09-06KC 130	1755	35	106.3	180	70
SPR09-06KC 135	1765	30	111.3	167	70
SPR09-06KC 140	1845	30	116.1	154	70
SPR09-06KC 145	1850	30	120.1	144	70
SPR09-06KC 155	1925	35	123.1	136	70
SPR09-06KC 160	1930	30	128.1	123	70
SPR09-06KC 166	2030	35	134.1	107	70
SPR09-06KC 170	2080	30	138.1	97	70
SPR09-06KC 175	2100	30	142.1	86	70
SPR09-06KC 180	2195	30	147.1	73	70
SPR09-06KC 185	2245	30	151.6	74	70
SPR09-06KC 199	2280	30	161.6	89	70
SPR09-06KC 206	2345	30	168.6	99	70
SPR09-06KC 211	2365	30	173.6	107	70
SPR09-06KC 240	2410	35	180.24	118	70
SPR09-06KC 245	2475	30	183.46	125	70
SPR09-06KC 250	2495	30	186.7	133	70
SPR09-06KC 254	2580	30	189.28	139	70
MV0811-14JC-1 49	2645	15	196.44	147	70
MV0811-14JC-1 58	2680	15	201.34	147	70
MV0811-14JC-1 68	2745	15	209.44	147	70
MV0811-14JC-1 80	2915	30	218.5	147	70
MV0811-14JC-2 15	2990	35	231.2	147	70
893A-1H-04 30	3130	80	240.794	147	70
MV0811-14JC-2 114	3135	15	244.98	147	70
MV0811-14JC-2 58	3325	30	259.18	147	70
MV0811-14JC-2 154	3415	15	262.78	147	70
MV0811-14JC-2 174	3460	15	276.74	147	70
MV0811-14JC-2 182.5	3590	15	282.56	147	70
MV0811-14JC-2 204	3780	15	297.22	147	70
MV0811-14JC-2 214	3915	15	307.22	147	70
MV0811-14JC-3 242	4085	15	328.48	147	70
MV0811-14JC-3 282	4225	20	349.48	147	70
MV0811-14JC-3 65	4315	30	360.42	147	70
MV0811-14JC-3 304	4365	15	368.86	147	70
MV0811-14JC-3 332	4475	15	382.84	147	70
MV0811-14JC-3 362	4670	15	405.34	147	70
MV0811-14JC-3 135	4670	35	406.34	147	70
893A-2H-01 55B	4740	70	411.095	147	70
MV0811-14JC-3 382	4810	15	425.34	147	70
MV0811-14JC-4 12	4995	15	437.38	147	70
MV0811-14JC-4 32	5170	20	454.94	147	70
MV0811-14JC-4 72	5230	15	473.1	147	70
MV0811-14JC-4 91	5400	15	489	147	70
MV0811-14JC-4 112	5585	20	509.74	147	70
MV0811-14JC-4 132	5760	20	529.74	147	70
MV0811-14JC-5 12	5965	15	542.9	147	70
893A-2H-02 71	6100	90	550.926	147	70
MV0811-14JC-6 14	6195	15	558.14	147	70

(*continued on next page*)

Table 2 (*continued*)

Lab ID	Age	Error	Depth	Mean reservoir age (yrs)	1 standard deviation error
MV0811-14JC-6 36	6415	15	576.32	147	70
MV0811-14JC-6 45	6450	15	584.92	147	70
MV0811-14JC-6 55	6515	20	591.18	147	70
MV0811-14JC-6 74	6570	20	599.22	147	70
MV0811-14JC-6 93	6710	20	616.5	147	70
MV0811-14JC-6 104	6815	20	627.5	147	70
MV0811-14JC-7 24	7155	20	673.48	147	70
MV0811-14JC-7 44	7420	15	686.06	147	70
893A-2H-04 18	7600	50	701.42	147	70
MV0811-14JC-7 64	7590	15	702.32	147	70
MV0811-14JC-7 86	7750	15	722.92	147	70
893A-2H-04 68	7910	70	736.495	147	70
MV0811-14JC-7 106	7995	20	742.92	147	70
893A-2H-04 93	8060	80	754.232	147	70
893A-2H-04 105B	8120	110	758.859	147	70
MV0811-14JC-7 126	8105	20	761.26	147	70
MV0811-14JC-7 146	8260	20	777.1	147	70
MV0811-14JC-8 8	8260	15	786.32	147	70
MV0811-14JC-8 26	8445	15	801.82	147	70
MV0811-14JC-8 47	8555	20	817.24	147	70

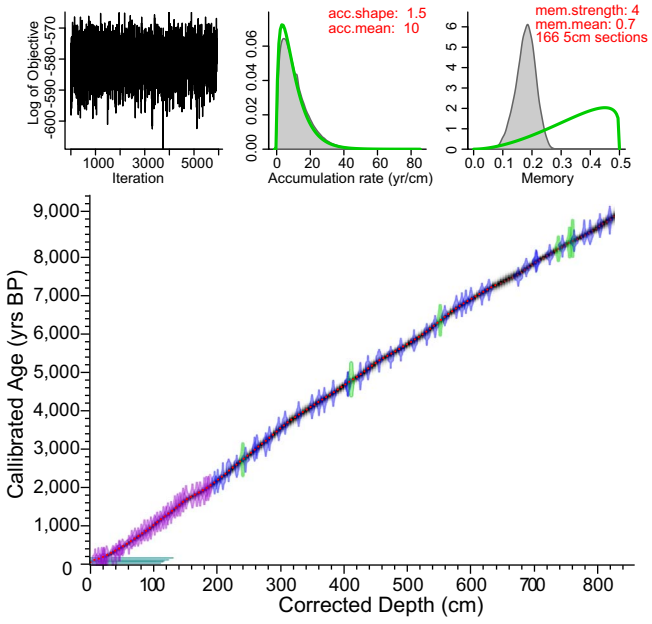

Fig. 2. BACON 2.2 output graph showing calibrated ^{14}C dates from MV0811-14JC (blue envelopes) SPR0901-06KC (purple) and ODP Hole 893A (green) and the age-depth model (gray shading indicates probability within the 95% confidence interval with darkness indicating greater probability; red curve shows single 'best' model based on the weighted mean age for each depth). (For interpretation of the references to colour in this figure legend, the reader is referred to the web version of this article.)

Gray and olive layers serve as stratigraphic tie points to correlate core MV0811-14JC to ODP Site 893 (Fig. 6). Some sedimentary segments are missing in ODP Site 893 between core sections which has been previously addressed by splicing ODP Hole 893A with Hole 893B. In contrast, MV0811-14JC was retrieved using a continuous coring technique resulting in a more complete record of gray and olive layers. Gray layers in core MV0811-14JC are comparable with gray layers in ODP site 893 except in the missing segments (i.e. ~6.8–7.9 m in ODP Hole 893A; ~11.1–11.4 m and ~11.7–13.7 m in ODP Hole 893B) (Fig. 6). There are offsets between cores in the depths and thicknesses of layers that are likely due to both coring differences (stratigraphic compression upon water loss and missing segments) between the cores and variations in the deposition of flood layers throughout the basin (Fig. 6). Olive layers are generally too obscure in the poorly resolved ODP core photos because of cracks or oxidization on the core surface but are clearly visible in scanned images of MV0811-14JC and SPR0901-03KC (Fig. 5). Rapid imaging after core splitting appears necessary to capture olive layers in SBB as oxidation of the sediments conceals the features of these layers. The dates of prominent gray and olive layers were estimated based on the improved age model presented here (Table 3).

4.3. Mass accumulation rates and sedimentation rates

The mass accumulation rate (MAR) of sediments closely follows the sedimentation rate (SR) during the last 9000 yrs. (Fig. 7d). The MAR of sediments decreases gradually from 200 to 90 g cm^{-2} kyr^{-1} between 9000 and 2500 yrs. BP. A sharp decrease (from 200 to 75 g cm^{-2} kyr^{-1}) occurred at ~6500 yrs. BP. The MAR rapidly increased to ~165 g cm^{-2} kyr^{-1} from 2300 to 1800 yr BP before decreasing again to ~90 g cm^{-2} ka^{-1} for 500 yrs. During the last 1400 yrs. the MAR increased dramatically from ~90 to ~280 g cm^{-2} kyr^{-1}.

5. Discussion

5.1. Chronology

The strong linear relationship between the ^{14}C dates from multiple cores and corrected depth (R^2 = 0.9956 in linear regression; Fig. 3) indicates that sedimentation in SBB is consistent through time. Additionally the linear relationship demonstrates the SBB stratigraphic record of gray layers can be used to correlate cores within the basin. Combining the cores (SPR0901-06KC, MV0811-14JC and core ODP Hole 893A) to generate an age-depth model using BACON 2.2 produces an average 95% confidence interval range of 236 yrs. through the record with a minimum of 144 yrs. at ~47 cm and a maximum of 372 yrs. at 825 cm (Fig. 2). Using this high-precision chronology, the well-dated stratigraphic pattern of gray and olive layers can now be applied to any SBB sediment cores to provide a readily available chronology.

However the age-depth relationship of the SBB sedimentary ^{14}C dates is not perfectly linear (Fig. 3). A consistent one-to-one relationship between the corrected age-depth relationship in SBB sediments and Marine13 calendar ages should exist if we assume an invariable reservoir age, a constant sedimentation rate and negligible differences in sediment compaction (i.e. via water loss) across the studied sections. Although the two curves are consistent prior to ~2500 yrs. BP, the SBB ^{14}C dates are generally ~200 yrs. older than the Marine13 calibration curve between 2500 and 8000 yrs. BP. Multiple reservoir ages probably

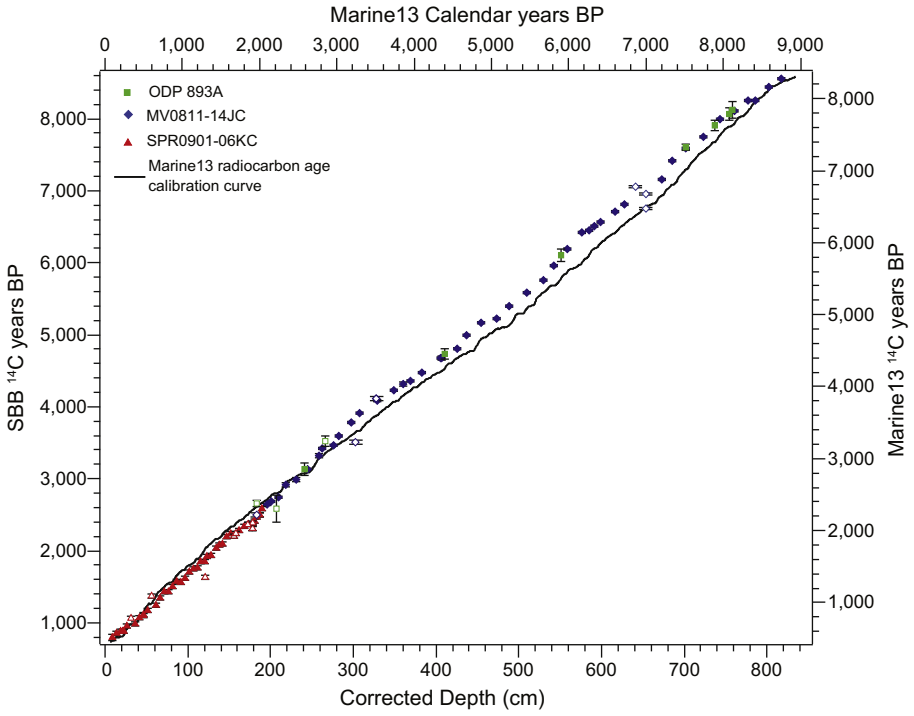

Fig. 3. Comparison of Santa Barbara Basin (SBB) dates and Marine13 calibration curve. Planktonic foraminiferal carbonate ^{14}C dates (reservoir age-corrected) from core SPR0901-06KC (solid red triangles), core MV0811-14JC (solid blue diamonds) and ODP Hole 893A (solid green squares) are plotted against depth corrected for instantaneous event thickness. Radiocarbon yrs. are plotted against calendar years on the Marine13 calibration curve (black line). Rejected dates are indicated by open symbols. (For interpretation of the references to colour in this figure legend, the reader is referred to the web version of this article.)

caused the strong covariation of the two age-depth curves prior to ~2500 yrs. BP. However, between 8000 and 2500 yrs. BP SBB either experienced greater surface ocean reservoir ages (> 550 years) or a decreased SR. Neither possibilities can be excluded as the SBB SR does show a general decrease between 9000 and 2500 yrs. BP (Fig. 7d) and the surface ocean reservoir age varied by ~350 yrs. during the last 2000 yrs. This result suggests further refinement of the SBB chronology is needed using independent dating methods such as terrestrial organic carbon ^{14}C dates matched to marine carbonate ^{14}C dates to determine reservoir age variability beyond the last 2000 yrs.

5.2. Flood events and mass accumulation rate

The stratigraphic record of SBB contains 75 gray layers deposited during the last 9000 yrs. Gray layers are characterized by high detrital elemental concentrations and significant increases in clay mineral abundance (Schimmelmann et al., 1998; Schimmelmann et al., 2003; Napier and Hendy, 2016), clayey silt or silty clay grain size without normal grading, high siliciclastic element concentrations (high Ti and low Ca/Ti) (Hendy et al., 2015), elevated terrestrial organic carbon abundance (lower δ^{13}C) (Schimmelmann and Kastner, 1993), a presence of fresh water diatoms (such as *Aulacoseira*) (Barron et al., 2015) and an absence of marine microfossils such as foraminifera (Schimmelmann et al., 2003). As these characteristics are typical of flood suspensates, the gray layers likely derived from suspended silt-size particles in large freshwater flood plumes that rapidly delivered siliciclastic sediments across the shelf to the center of the SBB (Thornton, 1984; Schimmelmann et al., 1998). Gray layers are therefore interpreted to be instantaneous events generated by extreme precipitation events in Southern California generating anomalous river runoff (Inman and Jenkins, 1999; Warrick et al., 2007; Romans et al., 2009; Covault et al., 2011).

Using the new age model, the number and thickness of gray layers per century was calculated to highlight changes in flood frequency and magnitude (Fig. 7b and c). The frequency and magnitude of floods generally increase during most of the high precipitation/run-off intervals indicated by multiple lacustrine records from Southern California between ~400–800, 3000–5500, 6600–7300 and 8500–9000 yrs. BP (Fig. 7a–c) (Kirby et al., 2010; Kirby et al., 2012; Kirby et al., 2014; Kirby et al., 2015; Hiner et al., 2016). The Holocene length records of increased C/N ratios from Lower Bear Lake (Kirby et al., 2012) and sand deposits in Lake Elsinore (Kirby et al., 2010) indicate high lake levels are consistent with intervals of greater flood frequency and magnitude in SBB at ~400, 3000, 6500 and 8500 yrs. BP (Fig. 7a–d). Additionally, elevated aridity between 650 and 1050 yrs. BP identified from tree-ring records of the western United States (Cook et al., 2004) occurred during the absence of gray layers. The concurrence of frequent (infrequent) gray layers and wetter (drier) climate indicates that flood events are likely to occur during wetter climate intervals suggesting the frequency of SBB gray layers might be utilized in paleoclimate reconstructions.

Although MAR and SR fluctuated during the last 9000 years, they both increase when the frequency and magnitude of flood layers increase (Fig. 7b–d). A statistically significant correlation ($r = 0.18$, $p = 0.016 < 0.05$) was found between MAR and sediment flux of floods (thickness of gray layers per century), confirming that a principal process driving sediment accumulation in SBB during the Holocene was precipitation (Warrick and Milliman, 2003). Approximately 85% of the central SBB sediment mass is composed of terrigenous sediments (Schwalbach and Gorsline, 1985) delivered by rivers. Precipitation plays a key role in weathering, erosion and transport of terrigenous sediments to depositional basins which contribute to changes in SR (Inman and Jenkins, 1999; Warrick et al., 2007; Romans et al., 2009; Covault et al., 2011; Gray et al., 2014;). Precipitation allows soil clay minerals to sorb water and disintegrate aggregates resulting in more mobile and erodible clay particles, which are available for run-off transport and are eventually deposited in the SBB (Bryan, 2000; Robert, 2004; Napier and Hendy, 2016). During extreme precipitation events and frequent winter storms, erosion is more intense, increasing the fluvial sediment load and terrigenous sediment delivery by the Santa Clara River, Ventura River and Santa Ynez Mountain streams to the SBB (Inman and Jenkins, 1999; Warrick et al., 2007; Romans et al., 2009; Covault et al., 2011). However, flood events are infrequent when extreme precipitation does not occur and river discharge is lower. Consequently, less terrestrial sediments are delivered to the SBB leading to decreased SR and MAR. However, although the relationship between

Table 3
Stratigraphy and chronology of gray and olive layers in core MV0811-14JC with layer notations. Ages are estimated using the age model derived from BACON 2.2.

Type of layer	Layer identification notation	Uncorrected depth of top (cm)	Uncorrected depth of bottom (cm)	Layer thickness (cm)	Corrected depth in core (cm)	Dates of events (Cal BP)	95% confidence ranges
Gray	1A	15.04	20.04	5.00	15.02	1912	1822–2006
Olive	1B	23.22	30.02	6.80	19.02	1950	1858–2046
Gray	2A	40.38	42.00	1.62	29.36	2065	1967–2165
Gray	2B	45.22	45.72	0.50	32.56	2105	2006–2205
Gray	2C	48.18	49.22	1.04	35	2134	2031–2246
Gray	2D	50.92	51.72	0.80	36.68	2155	2055–2260
Gray	2E	52.56	55.92	3.36	37.5	2165	2063–2269
Gray	2F	62.50	63.26	0.76	44.06	2250	2136–2364
Gray	2G	64.06	65.16	1.10	44.84	2259	2147–2377
Gray	2H	71.22	74.14	2.92	50.86	2336	2223–2461
Gray	2I	98.44	99.62	1.18	67.26	2564	2431–2689
Gray	2J	104.94	105.14	0.20	72.56	2636	2499–2751
Gray	2K	117.32	125.82	8.50	84.72	2794	2680–2915
Gray	2L	130.54	131.34	0.80	89.42	2860	2737–2999
Gray	2M	131.72	132.32	0.60	89.78	2865	2745–3001
Gray	2N	133.92	138.68	4.76	91.36	2887	2768–3017
Gray	2O	145.94	150.28	4.34	98.6	2986	2859–3116
Olive	3A	153.90	161.22	7.32	102.2	3038	2912–3162
Gray	3B	165.06	166.84	1.78	106.02	3090	2960–3217
Gray	3C	177.06	178.68	1.62	116.22	3219	3088–3340
Gray	3D	180.48	181.50	1.02	118	3242	3109–3360
Gray	3E	189.12	195.94	6.82	125.6	3353	3222–3476
Gray	3F	220.84	223.84	3.00	150.48	3698	3555–3837
Gray	3G	227.20	228.30	1.10	153.82	3737	3586–3881
Gray	3H	232.94	233.12	0.18	164.04	3855	3702–4001
Olive	4A	246.86	248.32	1.46	177.76	4005	3860–4149
Gray	4B	248.34	254.64	6.30	177.76	4005	3860–4149
Gray	4C	254.82	258.68	3.86	177.92	4007	3861–4151
Gray	4D	266.10	273.40	7.30	185.32	4084	3943–4221
Gray	4E	289.12	291.66	2.54	200.96	4252	4125–4373
Gray	4F	301.88	310.98	9.10	211.16	4358	4231–4476
Gray	4G	320.02	324.90	4.88	220.18	4454	4324–4579
Gray	4H	343.42	349.50	6.08	238.68	4658	4521–4780
Gray	5A	383.76	384.12	0.36	269.94	5008	4878–5147
Gray	5B	392.82	393.10	0.28	278.62	5119	4975–5257
Gray	5C	405.26	407.38	2.12	290.76	5263	5107–5392
Olive	5D	412.00	414.96	2.96	295.36	5317	5159–5441
Gray	5E	420.88	422.76	1.88	301.26	5376	5224–5495
Gray	5F	427.16	427.42	0.26	305.64	5416	5268–5536
Gray	5G	430.54	447.22	16.68	308.74	5444	5299–5561
Gray	5H	457.16	460.22	3.06	318.68	5537	5401–5651
Gray	5I	473.94	474.18	0.24	332.36	5673	5548–5791
Gray	6A	512.08	512.96	0.88	370.22	6079	5942–6204
Gray	6B	525.56	525.68	0.12	386	6286	6169–6403
Gray	6C	558.94	561.34	2.40	415.26	6664	6537–6781
Gray	6D	569.48	569.86	0.38	423.38	6754	6641–6859
Gray	6E	575.60	579.30	3.70	429.08	6811	6704–6916
Gray	6F	583.30	583.54	0.24	433.06	6851	6751–6953
Gray	6G	583.96	585.26	1.30	433.46	6855	6753–6958
Gray	6H	587.24	592.80	5.56	435.42	6875	6772–6980
Gray	7A	610.32	610.94	0.62	449.12	7008	6888–7125
Gray	7B	617.00	618.06	1.06	455.16	7068	6949–7185
Gray	7C	634.56	638.12	3.56	471.62	7222	7091–7336
Gray	7D	639.94	645.64	5.70	473.4	7238	7104–7356
Gray	7E	651.30	659.34	8.04	479.04	7286	7147–7421
Gray	7F	659.36	660.70	1.34	479.06	7287	7147–7421
Olive	7G	669.30	672.74	3.44	487.6	7361	7216–7501
Olive	7H	697.98	699.48	1.50	513.84	7587	7460–7719
Olive	7I	699.88	700.92	1.04	514.22	7590	7462–7723
Gray	7J	701.94	706.76	4.82	515.22	7600	7478–7730
Gray	7K	721.80	724.68	2.88	530.24	7770	7662–7880
Gray	7L	733.84	734.66	0.82	539.38	7867	7747–7977
Gray	7M	746.62	748.00	1.38	551.32	7988	7881–8092
Olive	8A	791.44	792.86	1.42	594.5	8397	8291–8499
Gray	8B	802.74	804.50	1.76	603.78	8475	8384–8577
Gray	8C	811.14	811.28	0.14	610.4	8533	8432–8643
Gray	8D	812.14	813.74	1.60	611.24	8540	8440–8649
Olive	8E	824.92	825.64	0.72	622.98	8644	8532–8765
Gray	8F	825.66	827.26	1.60	622.98	8644	8532–8765
Gray	8G	838.90	840.60	1.70	634.6	8753	8618–8898
Olive	8H	843.98	844.74	0.76	637.96	8790	8651–8935
Gray	8I	859.84	863.46	3.62	652.96	8950	8785–9108
Olive	8J	863.48	864.88	1.40	652.96	8950	8785–9108

(*continued on next page*)

Table 3 (*continued*)

Type of layer	Layer identification notation	Uncorrected depth of top (cm)	Uncorrected depth of bottom (cm)	Layer thickness (cm)	Corrected depth in core (cm)	Dates of events (Cal BP)	95% confidence ranges
Olive	8K	865.90	866.16	0.26	653.96	8961	8791–9122
Olive	8L	867.48	867.62	0.14	655.26	8974	8804–9136
Gray	9A	871.58	874.42	2.84	659.2	9014	8835–9183
Gray	9B	874.82	875.32	0.50	659.72	9019	8839–9189
Gray	9C	877.10	877.88	0.78	661.44	9037	8854–9211
Gray	9D	878.90	879.42	0.52	662.44	9048	8861–9224
Olive	9E	881.12	893.00	11.88	664.14	9065	8873–9251

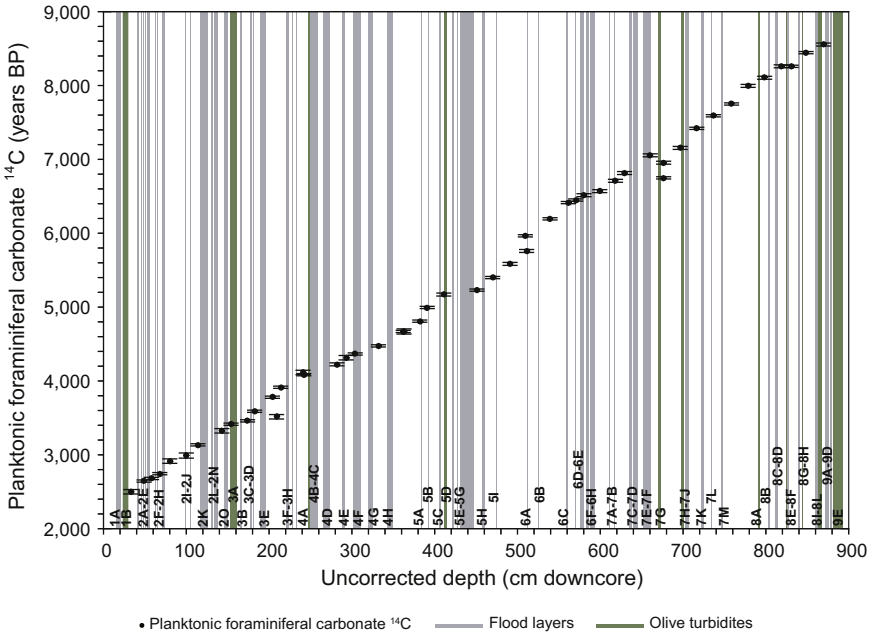

Fig. 4. Uncalibrated radiocarbon dates (solid circles) from core MV0811-14JC with 1σ analytical error (bars) plotted against uncorrected core depth. Stratigraphic markers including gray layers (light gray bars) and olive layers (dark green bars) are indicated and labeled using the notation from Table 3. (For interpretation of the references to colour in this figure legend, the reader is referred to the web version of this article.)

MAR and flood events was statistically significant, the correlation was only weak to moderate. Thus other factors must play a role in the delivery and accumulation of terrestrial sediments in SSB.

In addition to precipitation, vegetation cover also influences erosion in river catchments of Southern California because the rooting habit and density of vegetation are closely associated with hillside slope stability (Rice, 1969). The pollen record indicates that chaparral and coastal sage scrub community gradually increased during the Holocene, particularly since ~2300 yrs. BP and then decreased after 1300 CE before being replaced by grasses in the late 1700s (Heusser, 1978, 1998; Keeley, 2002; Ejarque et al., 2015; Heusser et al., 2015). Chaparral vegetation has stronger and deeper roots compared to grasses and can reduce erosion by enhancing slope stability (Hellmers et al., 1955; Gabet and Dunne, 2002) thus increased chaparral cover relative to grass could decrease the SR and MAR in SBB. Additionally, erosion can also be affected by the frequency of wildfires as the downslope movement rate of soil can be significantly increased when vegetation and litter are removed by fire (Florsheim et al., 1991; Kean et al., 2011; Kirby et al., 2014). However, no significant correlation was found in Zaca Lake between charcoal and runoff, indicating fire is not the dominant erosional process in the region (Kirby et al., 2014). Finally, earthquakes in tectonically active Southern California could increase SR and MAR in central SBB sediment by triggering easily erodible landslides in catchments or inducing considerable downslope displacement of marine sediments from the margin of the basin (Keefer, 1994; Wieczorek and Jager, 1996; Thunell et al., 1999).

5.3. Submarine downslope sediment processes and slumping

Nineteen massive olive layers were found in SBB laminated sediments during the last 9000 yrs. from core MV0811-14JC and SPR0901-03KC (olive layers in ODP Site 893 are no longer visible in the highly oxidized cores.). In contrast to gray layers, which are generated by flood events, the olive layers contain high Ca/Ti which is related to higher concentration of calcareous organisms – mainly foraminifera. This indicates that the olive layers contain marine-derived material (Hülsemann and Emery, 1961) and this observation is further supported by the appearance of benthic foraminiferal sands at the base of several of these layers (e.g., 1B and 3A). We interpret the olive layers as turbidites produced by fine-grained turbidity currents that originate from mass failure (e.g., debris-flows and submarine slides) on the upper slopes of SBB (Thornton, 1984; Rack and Merrill, 1995; Fisher et al., 2005). Sedimentary studies of Cariaco Basin found similar olive layers derived from turbidity flows (Peterson et al., 1991; Hughen et al., 1996). A seismically induced turbidity flow was observed in Cariaco Basin ~90 km from the rupture zone following a 6.8 earthquake in 1997. This downslope event was captured by transmissometer profiles, sediment traps and an associated box core and resulted in the downslope displacement of > 10^5 tons of sediments (Thunell et al., 1999).

Slope failure and subsequent turbidity currents have been associated with massive earthquakes on the North American Pacific Margin (Goldfinger et al., 2007) and more specifically in the tectonically active SBB (Fisher et al., 2005). The SBB lies within the San Andreas transform fault zone which contains many active faults (Toppozada et al., 2002) that could trigger slope failure within SBB and generate turbidity currents. One of the major earthquakes in California occurred around

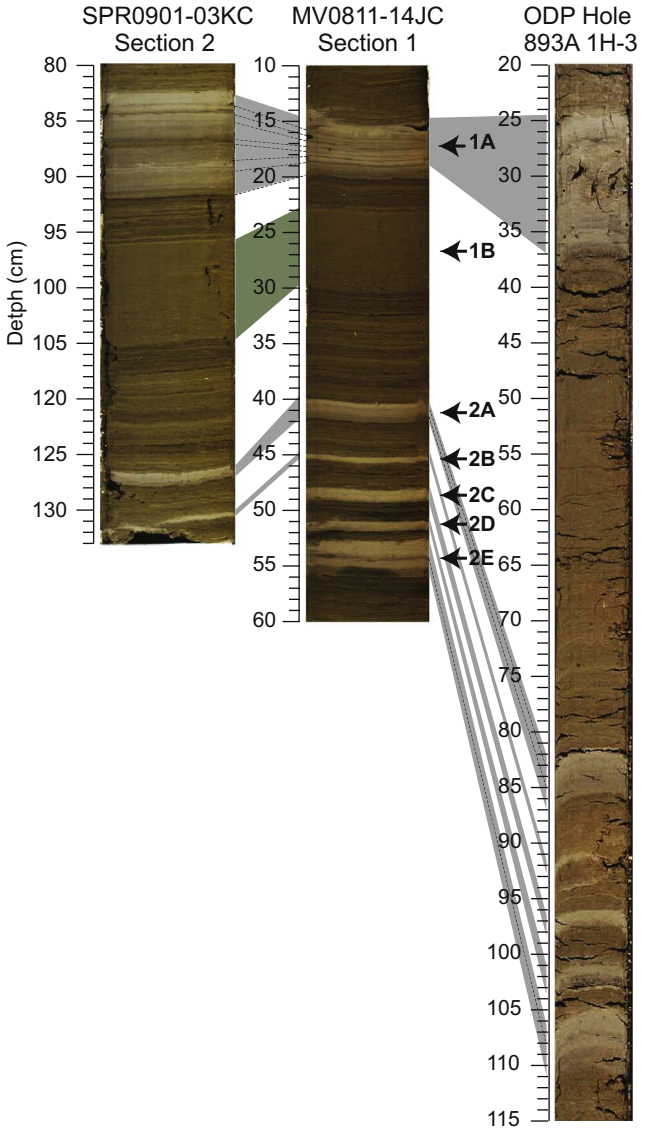

Fig. 5. Core image example of a typical segment of the correlation between cores MV0811-14JC, SPR0901-03KC and ODP Hole 893A. Gray and dark green shadings indicate the position and correlation of gray and olive layers, respectively. Core images were brightened to enhance the display of diagnostic colour differences. (For interpretation of the references to colour in this figure legend, the reader is referred to the web version of this article.)

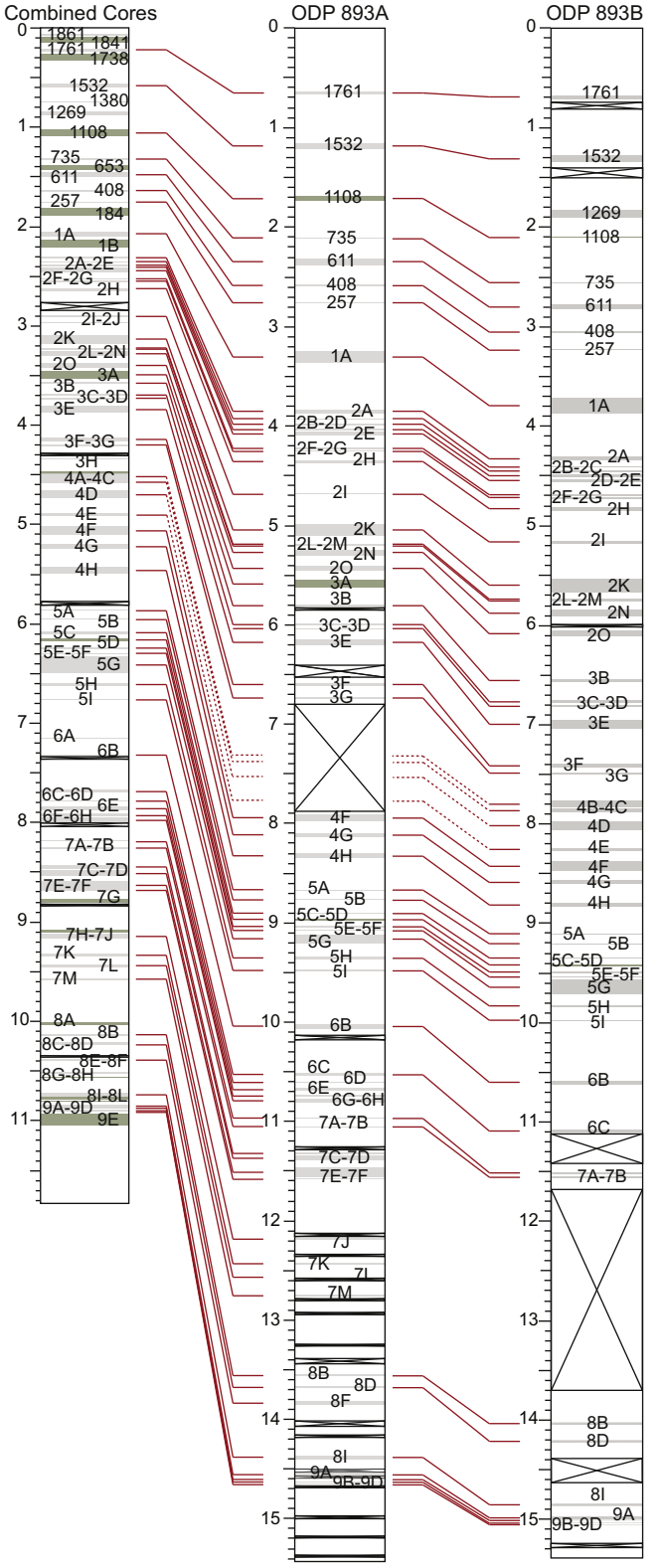

Fig. 6. Schematic stratigraphic correlation between combined cores SPR09-03KC and MV0811-14JC and ODP Holes 893A and 893B. The gray and dark green layers represent gray and olive layers respectively. Crossed boxes denote missing core material. Stratigraphic correlation between cores is indicated by red lines. Red dashed lines indicate where gray and olive layers are absent alongside missing core material. (For interpretation of the references to colour in this figure legend, the reader is referred to the web version of this article.)

Santa Barbara in 1811–1812 CE (Mission Quake) is reported to have produced a tsunami and probably generated submarine slope failure (Keefer, 1984; Borrero et al., 2001). The Mission Quake has been associated with turbidites of similar age in SBB and Santa Monica Basin (Schimmelmann et al., 1992; Gorsline, 1996). Furthermore, seismically induced slope failures and subsequent turbidity flows have been directly observed in association with several recent offshore earthquakes (Thunell et al., 1999; McHugh et al., 2011; Ashi et al., 2014) and marine turbidite stratigraphy has been widely used to record the history of significant offshore earthquakes in various regions (Gorsline, 1996; Goldfinger et al., 2007; McHugh et al., 2014).

Turbidites (olive layers) identified in core MV0811-14JC can be temporally linked to large earthquakes along the San Andreas Fault especially in the Transverse Ranges (listed in Table 4; Fig. 8). Four large Holocene coseismic uplift events resulted from slip on the Ventura – Pitas Point fault system, along the coast between Ventura and Carpinteria (Rockwell et al., 2016). Three of these emergence times, estimated at 955–1195 CE, 1850–2090 yrs. BP and 4150–4640 yrs. BP, can be

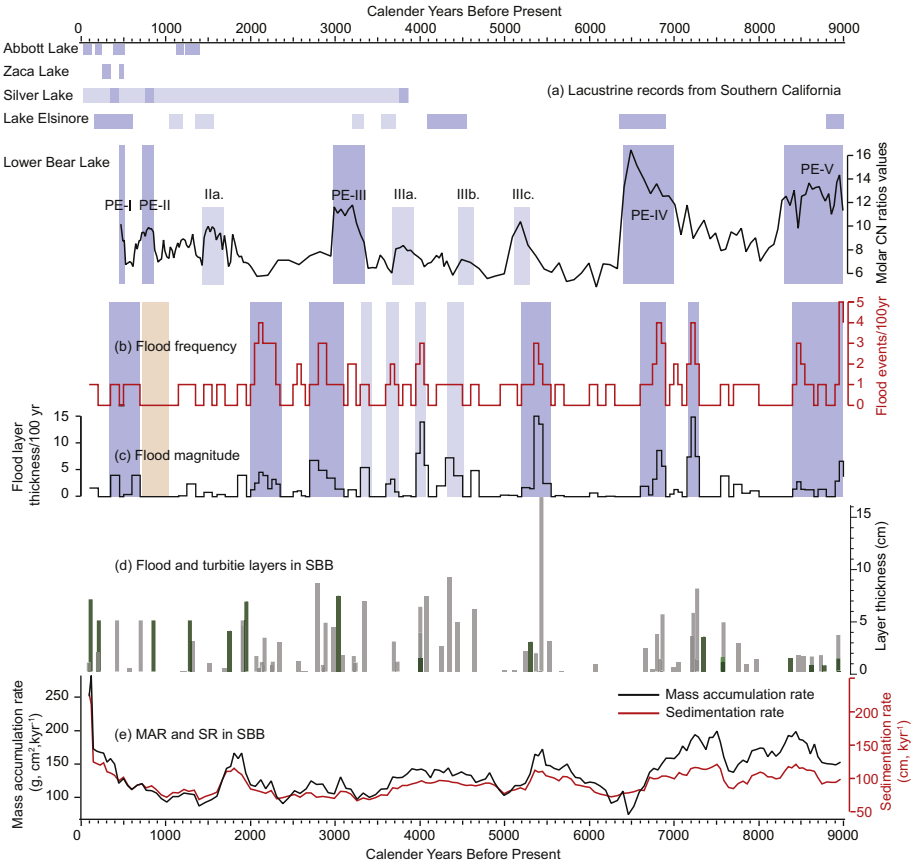

Fig. 7. Gray layer frequency and magnitude, SR and MAR in core MV0811-14JC and pluvial interval recorded from lakes in Southern California through the Holocene. (a) Lacustrine records from Abbott Lake (Hiner et al., 2016), Zaca Lake (Kirby et al., 2014), Silver Lake (Kirby et al., 2015) and Lake Elsinore (Kirby et al., 2010) in Southern California. Dark gray blocks refer to major, and light gray to minor pluvial episodes. Lower Bear Lake molar CN ratios are shown with pluvial episodes (PE) labeled (Kirby et al., 2012). (b) Flood frequency curve (flood events per century), (c) Flood magnitude (flood layer thickness per century) and (d) the thickness of gray (gray bars) and olive layers (dark green bars) in Santa Barbara Basin. (e) Sedimentation rate (SR; red line) and mass accumulation rate (MAR; blue line) calculated using the new chronology for Santa Barbara Basin. The dark gray bar shows wet intervals indicated by higher frequency and larger magnitude of flood events recorded in core MV0811-14JC. The light red bar shows an interval with elevated aridity found in tree-ring networks in the western United States (Cook et al., 2004). (For interpretation of the references to colour in this figure legend, the reader is referred to the web version of this article.)

related to turbidites generated at 1108 CE, 1950 yrs. BP (1B), and 4005 yrs. BP (4A) (Fig. 8). Two of these uplift events are also co-incident with large-magnitude earthquakes (after 1210 CE ± 75 and at 4000–4600 year BP) on the Ventura blind thrust fault (McAuliffe et al., 2015).The, large earthquakes on the Compton thrust fault, Los Angeles have less well resolved emergence times; those being 200–1250 years AD, 700–3400 years BP, 1900–3400 years BP, 5600–7200 years BP, 5400–8400 years BP (Leon et al., 2009), and therefore could be associated with a number of SBB turbidites (the olive layer at 184 CE, and layers 1B, 3A, 5D, 7G, and 7H; Fig. 8). Two late Holocene coseismic subsidence events (at 347–648 CE and 2085–1910 yrs. BP) resulting from large-magnitude earthquakes along the Newport-Inglewood fault could be related to turbidites at 653 CE and 1950 CE yrs. BP, respectively. Thus, marine turbidites in SBB can potentially be used to reconstruct the earthquake history in Southern California.

Additionally, evidence for the emplacement of a large slide is found at the base of core MV0811-14JC (sections 8–9) where laminated sediments are clearly not in situ as high-resolution core images show folding (section 9, Fig. S1 in Supplemental material). This segment is related to a series of age reversals (9070–10,325 yrs. BP) observed in section 2H-06 from ODP Hole 893A previously ascribed to slumped material (Nederbragt and Thurow, 2005). The stratigraphic disturbances could be the result of massive slope failure associated with submarine slides at the northern flank of SBB. The cores discussed here are located within ~1 km of the toe of the Goleta submarine slide complex western lobe whose offshore stratigraphy and geologic structure have been identified by multibeam bathymetric mapping and seismic-reflection data (Fig. 1) (Fisher et al., 2005; Greene et al., 2006;

Table 4
Turbidites (olive layers) identified in cores SPR09-03KC and MV0811-14JC with associated regional earthquake dates.

Layer identification notation	Turbidite age	Earthquake location	Earthquake age
1H[a]	1108 CE	Ventura–Pitas Point fault system[c]	955–1195 CE
		Ventura blind thrust fault[d]	1210 CE ± 75
2B[a]	653 CE	Newport-Inglewood fault system[b]	347–648 CE
2F[a]	184 CE	Compton thrust fault Los Angeles[e]	200–1250 CE
1B	1950 yrs. BP	Newport-Inglewood fault system[b]	2085–1910 yrs. BP
		Ventura–Pitas Point fault system[c]	1850–2090 yrs. BP
		Compton thrust fault[e]	700–3400 yrs. BP
3A	3038 yrs. BP	Compton thrust fault[e]	1900–3400 yrs. BP
4A	4005 yrs. BP	Ventura–Pitas Point fault system[c]	4150–4640 yrs. BP
		Ventura blind thrust fault[d]	4000–4600 yrs. BP

[a] Hendy et al. (2013).
[b] Leeper et al. (2017).
[c] Rockwell et al. (2016).
[d] McAuliffe et al. (2015).
[e] Leon et al. (2009).

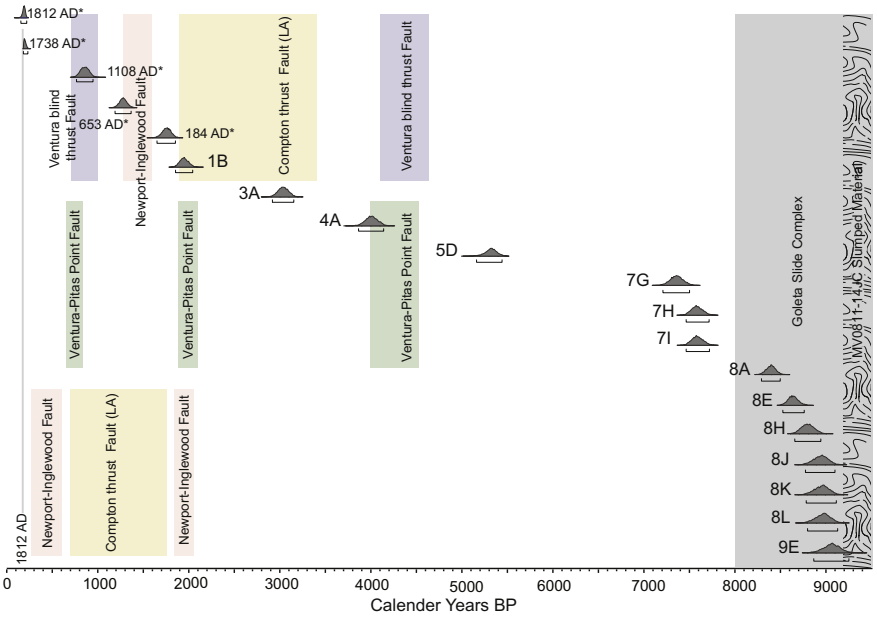

Fig. 8. Probability density functions (PDFs) for the 19 turbidites (olive layers) in core MV0811-14JC and core SPR090106KC in Santa Barbara Basin generated from Bacon 2.2. Brackets show 95% confidence intervals. Estimate emergence times of the Newport-Inglewood Fault (Leeper et al., 2017) in pink, Ventura-Pitas Point Fault (Rockwell et al., 2016) in green, Ventura blind thrust fault (McAuliffe et al., 2015) in purple, Compton Thrust Fault (Leon et al., 2009) in yellow and the Goleta Slide Complex (Fisher et al., 2005)in gray. Age of slumped material in 14JC is indicated by wavy texture. (For interpretation of the references to colour in this figure legend, the reader is referred to the web version of this article.)

Lee et al., 2009). Composed of slump blocks and mudflows, the submarine slide (14 km long and 11 km wide) originates from along the North Channel – Pitas Point – Red Mountain fault system and extends southwestward to a water depth of 570 m (Fisher et al., 2005; Greene et al., 2006).

Fisher et al. (2005) estimated the age of the central and western segments of the Goleta slide complex as ~ 8000 to 10,000 yrs. BP. based on the chronostratigraphy and oxygen-isotope record of ODP 893 core (Ingram and Kennett, 1995; Kennett, 1995) coupled with high resolution seismic-reflection data. The corresponding depth of the slide in ODP Hole 893A is ~15 mbct (m below core top) similar to the depth of the observed ^{14}C age reversals. Thus we constrain the slide's age to ~9000 yrs. BP ± 200 yrs. using the ^{14}C dates of laminated sediment sitting directly above the disturbed sediment in cores MV0811-14JC and ODP Hole 893A. Frequent turbidites are deposited in the millennia following the slump (Fig. 8) suggesting either slope stability was not quickly achieved after the slide or repeated triggering earthquakes occurred in the early Holocene.

Although regional earthquakes are the most obvious triggers for slope failure and turbidity currents, other processes could enhance the frequency of such events, especially rapid sediment accumulation (Gorsline, 1996; Fisher et al., 2005; Greene et al., 2006; Lee et al., 2009). During a major flood event, the discharge of Santa Clara River (accounting for the ~80% of sediment flux to the SBB) can approach 10^7 to 10^8 m^3 resulting in a total sediment discharge of 10^2 to 10^3 kt (Warrick et al., 2004). Flood sediment initially deposited on the shelf can subsequently be resuspended and transported to the central SBB by waves and currents, or can be temporarily loaded on slopes that will ultimately fail and generate turbidity currents (Gorsline, 1996). Evidence for these processes can be found in MV0811-14JC. Olive layer 8E directly overlays a thick gray layer (8F) suggesting a turbidity current derived from slope failure subsequent to a significant flood event (Fig. S1). Other processes such as high fluid pressures and oversteepening may also impact sediment on shelf slopes and contribute to slope failure. Further investigation of massive olive layers in laminated SBB sediments is necessary to determine whether the slope failure is triggered by tectonic activity and/or rapid sediment delivery.

6. Conclusion

High-resolution radiocarbon measurements of mixed planktonic foraminifera from core MV0811-14JC in combination with ^{14}C dates from SPR0901-06KC and ODP Hole 893A provide a revised chronology for the SBB sedimentary record over last 9000 yrs. Prominent gray and olive layers identified in multiple cores allowed for stratigraphic correlation between cores. The age of these stratigraphic markers has been estimated using the revised chronology providing a readily available chronology for future SBB coring efforts. Gray layers are interpreted to be the product of floods associated with extreme precipitation events. The frequency of flood layers was calculated and frequent (infrequent) floods were found during generally wetter (drier) intervals identified by Southern California hydroclimate reconstructions. Both mass accumulation rate and sedimentation rate increase when floods are frequent indicating that Holocene sedimentation accumulation in SBB is influenced by precipitation.

A second type of massive sedimentary event was identified in the SBB stratigraphic sequence. Olive layers are interpreted as turbidities derived from downslope displacement of sediments. Although not all downslope events are associated with seismic activity, the newly identified olive layers are well dated and can potentially be used to reconstruct the earthquake history in Southern California. A slump related to the Goleta submarine slide complex was identified at the base of MV0811-14JC by folded sediments in high-resolution core images. Core-to-core correlation with ODP Hole 893A places these disturbed sediments within ^{14}C age reversals in ODP Hole 893A which serve as evidence for sediment displacement around 9000 ± 200 yrs. Our improved radiocarbon chronology for the past 9000 yrs. of sedimentation in SBB together with the identified gray and olive layers provide a valuable well constrained and easily accessible stratigraphy for future high-resolution core-to-core correlations and thus enhance the value of SBB sediment for paleoceanographic and paleoclimatic studies.

Supplementary data to this article can be found online at https://doi.org/10.1016/j.margeo.2017.11.014.

Acknowledgments

This work is supported by the National Science Foundation under grant number OCE-1304327 (I.H.) and OCE-0752068 (A.S.). We gratefully acknowledge the captain and crew of the R/V Melville, and Co-Chiefs Richard Behl and James Kennett for collection of the core MV0811-14JC. We would like to thank John Southon at the Keck Carbon Cycle Accelerator Mass Spectrometer University of California Irvine for assisting in ^{14}C dating. We acknowledge Tiffany J. Napier and Yi Wang for their aid in sample preparation.

References

Ashi, J., Sawada, R., Omura, A., Ikehara, K., 2014. Accumulation of an earthquake-induced extremely turbid layer in a terminal basin of the Nankai accretionary prism. Earth Planets Space 66, 51.

Barron, J.A., Bukry, D., Hendy, I.L., 2015. High-resolution paleoclimatology of the Santa Barbara Basin during the Medieval Climate Anomaly and early Little Ice Age based on diatom and silicoflagellate assemblages in Kasten core SPR0901-02KC. Quat. Int. 387, 13–22.

Behl, R.J., 1995. 22. Sedimentary facies and sedimentology of the late Quaternary Santa Barbara Basin, site 893. Proc. Ocean Drill. Program Sci. Results 146 (Pt. 2), 295–308.

Beverly, R.K., Beaumont, W., Tauz, D., Ormsby, K.M., von Reden, K.F., Santos, G.M., Southon, J.R., 2010. The Keck carbon cycle AMS Laboratory, University of California, Irvine: status report. Radiocarbon 52, 301–309.

Blaauw, M., Christen, J.A., 2011. Flexible paleoclimate age-depth models using an autoregressive gamma process. Bayesian Anal. 6, 457–474.

Borrero, J.C., Dolan, J.F., Synolakis, C.E., 2001. Tsunamis within the eastern Santa Barbara Channel. Geophys. Res. Lett. 28, 643–646.

Bryan, R.B., 2000. Soil erodibility and processes of water erosion on hillslope. Geomorphology 32, 385–415.

Cook, E.R., Woodhouse, C.A., Eakin, C.M., Meko, D.H., Stahle, D.W., 2004. Long-term aridity changes in the western United States. Science 306, 1015–1018.

Covault, J.A., Romans, B.W., Graham, S.A., Fildani, A., Hilley, G.E., 2011. Terrestrial source to deep-sea sink sediment budgets at high and low sea levels: insights from tectonically active Southern California. Geology 39, 619–622.

Duvall, A., Kirby, E., Burbank, D., 2004. Tectonic and lithologic controls on bedrock channel profiles and processes in coastal California. J. Geophys. Res. Earth Surf. 109.

Ejarque, A., Anderson, R.S., Simms, A.R., Gentry, B.J., 2015. Prehistoric fires and the shaping of colonial transported landscapes in southern California: a paleoenvironmental study at Dune pond, Santa Barbara County. Quat. Sci. Rev. 112, 181–196.

Fisher, M.A., Normark, W.R., Greene, H.G., Lee, H.J., Sliter, R.W., 2005. Geology and tsunamigenic potential of submarine landslides in Santa Barbara Channel, Southern California. Mar. Geol. 224, 1–22.

Fisler, J., Hendy, I.L., 2008. California current system response to late Holocene climate cooling in southern California. Geophys. Res. Lett. 35, L09702.

Fleischer, P., 1972. Mineralogy and sedimentation history, Santa Barbara Basin, California. J. Sediment. Petrol. 42, 49–58.

Florsheim, J.L., Keller, E.A., Best, D.W., 1991. Fluvial sediment transport in response to moderate storm flows following chaparral wildfire, Ventura County, Southern California. Geol. Soc. Am. Bull. 103, 504–511.

Gabet, E.J., Dunne, T., 2002. Landslides on coastal sage-scrub and grassland hillslopes in a severe El Niño winter: the effects of vegetation conversion on sediment delivery. Geol. Soc. Am. Bull. 114, 983–990.

Goldfinger, C., Morey, A.E., Nelson, C.H., Gutiérrez-Pastor, J., Johnson, J.E., Karabanov, E., Chaytor, J., Eriksson, A., Party, S.S., 2007. Rupture lengths and temporal history of significant earthquakes on the offshore and north coast segments of the northern San Andreas fault based on turbidite stratigraphy. Earth Planet. Sci. Lett. 254, 9–27.

Gorsline, D.S., 1996. Depositional events in Santa Monica Basin, California borderland, over the past five centuries. Sediment. Geol. 104, 73–88.

Gray, A.B., Warrick, J.A., Pasternack, G.B., Watson, E.B., Goni, M.A., 2014. Suspended sediment behavior in a coastal dry-summer subtropical catchment: effects of hydrologic preconditions. Geomorphology 214, 485–501.

Greene, H.G., Murai, L.Y., Watts, P., Maher, N.A., Fisher, M.A., Paull, C.E., Eichhubl, P., 2006. Submarine landslides in the Santa Barbara Channel as potential tsunami sources. Nat. Hazards Earth Syst. Sci. 6, 63–88.

Heck, R.G., 1998. Santa Barbara Channel regional formline map, top Monterey Formation. In: Kunitomi, D.S., Hopps, T.E., Galloway, J.M. (Eds.), Structure and petroleum geology. Santa Barbara Channel, California, Miscellaneous Publication, vol. 46. Pacific Section American Association Petroleum Geologists and Coast Geological Society, Bakersfield, CA, pp. 183–184 1 sheet.

Hellmers, H., Horton, J.S., Juhren, G., O'keefe, J., 1955. Root systems of some Chaparral Plants in Southern California. Ecology 36, 667–678.

Hendy, I.L., Dunn, L., Schimmelmann, A., Pak, D.K., 2013. Resolving varve and radiocarbon chronology differences during the last 2000 years in the Santa Barbara Basin sedimentary record, California. Quat. Int. 310, 155–168.

Hendy, I.L., Napier, T.J., Schimmelmann, A., 2015. From extreme rainfall to drought: 250 years of annually resolved sediment deposition in Santa Barbara Basin, California. Quat. Int. 387, 3–12.

Heusser, L., 1978. Pollen in Santa Barbara Basin, California: a 12,000-yr record. Geol. Soc. Am. Bull. 89, 673–678.

Heusser, L., 1998. Direct correlation of millennial-scale changes in western North American vegetation and climate with changes in the California current system over the past similar to 60 kyr. Paleoceanography 13, 252–262.

Heusser, L.E., Hendy, I.L., Barron, J.A., 2015. Vegetation response to southern California drought during the Medieval Climate Anomaly and early Little Ice Age (AD 800–1600). Quat. Int. 387, 23–35.

Hiner, C.A., Kirby, M.E., Bonuso, N., Patterson, W.P., Palermo, J., Silveira, E., 2016. Late Holocene hydroclimatic variability linked to Pacific forcing: evidence from Abbott Lake, coastal central California. J. Paleolimnol. 56, 299–313.

Hughen, K.A., Overpeck, J.T., Peterson, L.C., Anderson, R.F., 1996. The nature of varved sedimentation in the Cariaco Basin, Venezuela, and its palaeoclimatic significance. Geol. Soc. Lond., Spec. Publ. 116 (1), 171–183.

Hülsemann, J., Emery, K.O., 1961. Stratification in recent sediments of Santa-Barbara Basin as controlled by organisms and water character. J. Geol. 69, 279–290.

Ingram, B.L., Kennett, D.J., 1995. Radiocarbon chronology and planktonic–benthic foraminifera 14C age differences in Santa Barbara Basin sediments, hole 893A. Proc. Ocean Drill. Program Sci. Results 146 (Pt. 2), 19–27.

Inman, D.L., Jenkins, S.A., 1999. Climate change and the episodicity of sediment flux of small California rivers. J. Geol. 107, 251–270.

Kean, J.W., Staley, D.M., Cannon, S.H., 2011. In situ measurements of post-fire debris flows in southern California: comparisons of the timing and magnitude of 24 debris-flow events with rainfall and soil moisture conditions. J. Geophys. Res. Earth Surf. 116 (F4).

Keefer, D.K., 1984. Landslides caused by earthquakes. Geol. Soc. Am. Bull. 95, 406–421.

Keefer, D.K., 1994. The importance of earthquake-induced landslides to long-term slope erosion and slope-failure hazards in seismically active regions. Geomorphology 10, 265–284.

Keeley, J.E., 2002. Native American impacts on fire regimes of the California coastal ranges. J. Biogeogr. 29, 303–320.

Kennett, P.J., 1995. 1. Latest Quaternary benthic oxygen and carbon isotope stratigraphy: hole 893A, Santa Barbara Basin, California. Proc. Ocean Drill. Program Sci. Results 146 (Pt. 2), 3–18.

Kennett, J.P., Venz, K., 1995. 21. Late Quaternary climatically related planktonic foraminiferal assemblage changes: hole 893A, Santa Barbara Basin, California. Proc. Ocean Drill. Program Sci. Results 146 (Pt. 2), 281–294.

Kirby, M.E., Lund, S.P., Patterson, W.P., Anderson, M.A., Bird, B.W., Ivanovici, L., Monarrez, P., Nielsen, S., 2010. A Holocene record of Pacific decadal oscillation (PDO)-related hydrologic variability in Southern California (Lake Elsinore, CA). J. Paleolimnol. 44, 819–839.

Kirby, M.E., Zimmerman, S.R.H., Patterson, W.P., Rivera, J.J., 2012. A 9170-year record of decadal-to-multi-centennial scale pluvial episodes from the coastal Southwest United States: a role for atmospheric rivers? Quat. Sci. Rev. 46, 57–65.

Kirby, M.E., Feakins, S.J., Hiner, C.A., Fantozzi, J., Zimmerman, S.R.H., Dingemans, T., Mensing, S.A., 2014. Tropical Pacific forcing of late-Holocene hydrologic variability in the coastal southwest United States. Quat. Sci. Rev. 102, 27–38.

Kirby, M.E., Knell, E.J., Anderson, W.T., Lachniet, M.S., Palermo, J., Eeg, H., Lucero, R., Murrieta, R., Arevalo, A., Silveira, E., Hiner, C.A., 2015. Evidence for insolation and Pacific forcing of late glacial through Holocene climate in the central Mojave Desert (Silver Lake, CA). Quat. Res. 84, 174–186.

Kolpack, R.L., Drake, D.E., 1984. Transport of clays in the eastern part of Santa-Barbara Channel, California. Geo-Mar. Lett. 4, 191–196.

Lange, C.B., Schimmelmann, A., 1995. 26. Data report: x-radiography of selected, predominantly varved intervals at hole 893A. Proc. Ocean Drill. Program Sci. Results 146 (Pt. 2), 333–346.

Lange, C.B., Berger, W.H., Burke, S.K., Casey, R.E., Schimmelmann, A., Soutar, A., Weinheimer, A.L., 1987. El Niño in Santa Barbara Basin: diatom, radiolarian and foraminiferan responses to the "1983 El Niño" event. Mar. Geol. 78, 153–160.

Lee, H.J., Greene, H.G., Edwards, B.D., Fisher, M.A., Normark, W.R., 2009. Submarine landslides of the Southern California borderland. Earth Science in the Urban Ocean: The Southern California Continental Borderland: Geol. Soc. Am. Spec. Pap. 454, 251–269.

Leeper, R., Rhodes, B., Kirby, M., Scharer, K., Carlin, J., Hemphill-Haley, E., Avnaim-Katav, S., MacDonald, G., Starratt, S., Aranda, A., 2017. Evidence for coseismic subsidence events in a southern California coastal saltmarsh. Sci. Rep. 7, 44615.

Leon, L.A., Dolan, J.F., Shaw, J.H., Pratt, T.L., 2009. Evidence for large holocene earthquakes on the compton thrust fault, Los Angeles, California. J. Geophys. Res. Solid Earth 114.

Lynn, R.J., Simpson, J.J., 1987. The California current system - the seasonal variability of its physical characteristics. J. Geophys. Res. Oceans 92, 12947–12966.

Marshall, S.T., Funning, G.J., Krueger, H.E., Owen, S.E., Loveless, J.P., 2017. Mechanical models favor a ramp geometry for the Ventura-pitas point fault, California. Geophys. Res. Lett. 44, 1311–1319.

Mayewski, P.A., Rohling, E.E., Stager, J.C., Karlen, W., Maasch, K.A., Meeker, L.D., Meyerson, E.A., Gasse, F., van Kreveld, S., Holmgren, K., Lee-Thorp, J., Rosqvist, G., Rack, F., Staubwasser, M., Schneider, R.R., Steig, E.J., 2004. Holocene climate variability. Quat. Res. 62, 243–255.

McAuliffe, L.J., Dolan, J.F., Rhodes, E.J., Hubbard, J., Shaw, J.H., Pratt, T.L., 2015. Paleoseismologic evidence for large-magnitude (MW 7.5-8.0) earthquakes on the Ventura blind thrust fault: implications for multifault ruptures in the transverse ranges of southern California. Geosphere 11, 1629–1650.

McHugh, C.M., Seeber, L., Braudy, N., Cormier, M.H., Davis, M.B., Diebold, J.B., Dieudonne, N., Douilly, R., Gulick, S.P.S., Hornbach, M.J., Johnson, H.E., Mishkin, K.R., Sorlien, C.C., Steckler, M.S., Symithe, S.J., Templeton, J., 2011. Offshore sedimentary effects of the 12 January 2010 Haiti earthquake. Geology 39, 723–726.

McHugh, C.M.G., Seeber, L., Cormier, M.H., Hornbach, M., 2014. Submarine Paleoseismology along populated transform boundaries: the Enriquillo-plantain-garden fault, Canal du Sud, Haiti, and the north Anatolian fault, Marmara Sea, Turkey. Oceanography 27, 118–131.

Napier, T.J., Hendy, I.L., 2016. The Impact of Hydroclimate and Dam Construction on Terrigenous Detrital Sediment Composition in a 250-Year Santa Barbara Basin Record off Southern California. (Quaternary International).

Nederbragt, A.J., Thurow, J., 2005. Geographic coherence of millennial-scale climate cycles during the Holocene. Palaeogeogr. Palaeoclimatol. Palaeoecol. 221, 313–324.

Peterson, L.C., Overpeck, J.T., Kipp, N.G., Imbrie, J., 1991. A high-resolution late Quaternary upwelling record from the anoxic Cariaco Basin, Venezuela. Paleoceanography 6, 99–119.

Rack, F.R., Merrill, R.B., 1995. 12. Santa Barbara Basin: construction of a 16,000-year composite record using magnetic susceptibility and digital color imaging data. Proc. Ocean Drill. Program Sci. Results 146 (Pt. 2), 169–192.

Reimer, P.J., Bard, E., Bayliss, A., Beck, J.W., Blackwell, P.G., Ramsey, C.B., Buck, C.E., Cheng, H., Edwards, R.L., Friedrich, M., Grootes, P.M., Guilderson, T.P., Haflidason,

H., Hajdas, I., Hatte, C., Heaton, T.J., Hoffmann, D.L., Hogg, A.G., Hughen, K.A., Kaiser, K.F., Kromer, B., Manning, S.W., Niu, M., Reimer, R.W., Richards, D.A., Scott, E.M., Southon, J.R., Staff, R.A., Turney, C.S.M., van der Plicht, J., 2013. IntCal13 and Marine13 radiocarbon age calibration curves 0–50,000 years cal BP. Radiocarbon 55, 1869–1887.

Rice, R.M., 1969. Soil slips related to vegetation, topography, and soil in southern California. Water Resour. Res. 5, 647–659.

Roark, E.B., Ingram, B.L., Southon, J., Kennett, J.P., 2003. Holocene foraminiferal radiocarbon record of paleocirculation in the Santa Barbara Basin. Geology 31, 379–382.

Robert, C., 2004. Late Quaternary variability of precipitation in Southern California and climatic implications: clay mineral evidence from the Santa Barbara Basin, ODP site 893. Quat. Sci. Rev. 23, 1029–1040.

Rockwell, T.K., Clark, K., Gamble, L., Oskin, M.E., Haaker, E.C., Kennedy, G.L., 2016. Large transverse range earthquakes cause coastal upheaval near Ventura, Southern California. Bull. Seismol. Soc. Am. 106, 2706–2720.

Romans, B.W., Normark, W.R., McGann, M.M., Covault, J.A., Graham, S.A., 2009. Coarse-grained sediment delivery and distribution in the Holocene Santa Monica Basin, California: implications for evaluating source-to-sink flux at millennial time scales. Geol. Soc. Am. Bull. 121, 1394–1408.

Schimmelmann, A., Kastner, M., 1993. Evolutionary changes over the last 1000 years of reduced sulfur phases and organic carbon in varved sediments of the Santa Barbara Basin, California. Geochim. Cosmochim. Acta 57, 67–78.

Schimmelmann, A., Lange, C.B., Berger, W.H., Simon, A., Burke, S.K., Dunbar, R.B., 1992. Extreme climatic conditions recorded in Santa Barbara Basin laminated sediments: the 1835–1840 Macoma event. Mar. Geol. 106, 279–299.

Schimmelmann, A., Zhao, M., Harvey, C.C., Lange, C.B., 1998. A large California flood and correlative global climatic events 400 years ago. Quat. Res. 49, 51–61.

Schimmelmann, A., Lange, C.B., Meggers, B.J., 2003. Palaeoclimatic and archaeological evidence for a similar to 200-yr recurrence of floods and droughts linking California, Mesoamerica and South America over the past 2000 years. The Holocene 13, 763–778.

Schimmelmann, A., Lange, C.B., Roark, E.B., Ingram, B.L., 2006. Resources for paleo-ceanographic and paleoclimatic analysis: a 6,700-year stratigraphy and regional radiocarbon reservoir-age (ΔR) record based on varve counting and 14C-AMS dating for the Santa Barbara Basin, offshore California, U.S.A. J. Sediment. Res. 76, 74–80.

Schimmelmann, A., Hendy, I.L., Dunn, L., Pak, D.K., Lange, C.B., 2013. Revised ~ 2000-year chronostratigraphy of partially varved marine sediment in Santa Barbara Basin, California. Geologiska Föreningen i Stockholm Förhandlingar (GFF) 135, 258–264.

Schimmelmann, A., Lange, C.B., Schieber, J., Francus, P., Ojala, A.E.K., Zolitschka, B., 2016. Varves in marine sediments: a review. Earth Sci. Rev. 159, 215–246.

Schwalbach, J.R., Gorsline, D.S., 1985. Holocene sediment budgets for the basins of the California continental borderland. J. Sediment. Petrol. 55, 829–842.

Soutar, A., Crill, P.A., 1977. Sedimentation and climatic patterns in the Santa Barbara Basin during the 19th and 20th centuries. Geol. Soc. Am. Bull. 88, 1161–1172.

Thornton, S.E., 1984. Basin model for hemipelagic sedimentation in a tectonically active continental margin: Santa Barbara Basin, California continental borderland. Geol. Soc. Spec. Publ. 377–394.

Thunell, R.C., 1998. Particle fluxes in a coastal upwelling zone: sediment trap results from Santa Barbara Basin, California. Deep Sea Res. Part 2 Top. Stud. Oceanogr. 45, 1863–1884.

Thunell, R., Tappa, E., Varela, R., Llano, M., Astor, Y., Muller-Karger, F., Bohrer, R., 1999. Increased marine sediment suspension and fluxes following an earthquake. Nature 398, 233–236.

Toppozada, T.R., Branum, D.M., Reichle, M.S., Hallstrom, C.L., 2002. San Andreas fault zone, California: M ≥ 5.5 earthquake history. Bull. Seismol. Soc. Am. 92, 2555–2601.

Wanner, H., Beer, J., Butikofer, J., Crowley, T.J., Cubasch, U., Fluckiger, J., Goosse, H., Grosjean, M., Joos, F., Kaplan, J.O., Kuttel, M., Muller, S.A., Prentice, I.C., Solomina, O., Stocker, T.F., Tarasov, P., Wagner, M., Widmann, M., 2008. Mid- to late Holocene climate change: an overview. Quat. Sci. Rev. 27, 1791–1828.

Warrick, J.A., Mertes, L.A.K., 2009. Sediment yield from the tectonically active semiarid western transverse ranges of California. Geol. Soc. Am. Bull. 121, 1054–1070.

Warrick, J.A., Milliman, J.D., 2003. Hyperpycnal sediment discharge from semiarid southern California rivers: implications for coastal sediment budgets. Geology 31, 781–784.

Warrick, J.A., Mertes, L.A.K., Washburn, L., Siegel, D.A., 2004. A conceptual model for river water and sediment dispersal in the Santa Barbara Channel, California. Cont. Shelf Res. 24, 2029–2043.

Warrick, J.A., DiGiacomo, P.M., Weisberg, S.B., Nezlin, N.P., Mengel, M., Jones, B.H., Ohlmann, J.C., Washburn, L., Terrill, E.J., Farnsworth, K.L., 2007. River plume patterns and dynamics within the Southern California Bight. Cont. Shelf Res. 27, 2427–2448.

Weinheimer, A.L., Cayan, D.R., 1997. Radiolarian assemblages from Santa Barbara Basin sediments: recent interdecadal variability. Paleoceanography 12, 658–670.

Wieczorek, G.F., Jager, S., 1996. Triggering mechanisms and depositional rates of post-glacial slope-movement processes in the Yosemite valley, California. Geomorphology 15, 17–31.